Renovating phase constitution and construction of Pt nanocubes for electrocatalysis of methanol oxidation via a solvothermal-induced strong metal-support interaction

Yi Wang [a], Zhaohong Li [a], Xingqun Zheng [b,c,**], Rui Wu [d], Jianfeng Song [a], Yulin Chen [a], Xinzhe Cao [a], Yi Wang [a], Yao Nie [a,*]

[a] *Chongqing Key Laboratory of Green Synthesis and Applications, College of Chemistry, Chongqing Normal University, Chongqing 401331, China*
[b] *College of Safety Engineering, Chongqing University of Science & Technology, Chongqing 401331, China*
[c] *The State Key Laboratory of Power Transmission Equipment & System Security and New Technology, College of Chemistry and Chemical Engineering, Chongqing University, Chongqing 400044, China*
[d] *School of Materials and Energy, University of Electronic Science and Technology of China, Chengdu 610054, China*

ARTICLE INFO

ABSTRACT

Strong metal-support interaction (SMSI) covering migration of reducible oxides from the support onto loaded metal surfaces and alloying of the guest metal with the metal component in the support displays important roles in tuning catalytic behavior. While conventional construction of SMSI involves high-temperature redox treatment and cannot ensure simultaneous appearance of oxide migration and alloying mechanisms, limiting the function and application of SMSI in electrocatlysis. Herein, a low-temperature solvothermal-induced SMSI is established in the $CeCuO_x/C$ supported Pt system, where the partial encapsulation of supported Pt by CeO_x and the alloying of Cu^{2+} in the substrate with guest Pt occur readily and simultaneously. Such encapsulation and alloying processes completely refurbish the catalysis configuration and restructure the geometric/electronic state of interfacial Pt atoms, endowing the $CeO_x/PtCu/CeCuO_x/C$ product with modulated adsorption energies toward reactive intermediates and consequently much enhanced performance for methanol oxidation reaction (MOR).

1. Introduction

Platinum (Pt) has been the most efficient metal catalyst for methanol oxidation reaction (MOR) [1,2]. However, its high price, sluggish kinetics, poor long-term stability and surface CO poisoning seriously restrict its practical application and delay the widespread deployment of related liquid fuel cell technologies [3,4]. In the electrocatalysis, the performance of Pt is determined by its electronic structure, which sensitively depends on phase compositions and structures[5–7]. Creating effective carrier effect is one of effective strategies to induce electronic modifications to Pt [8–10]. However, mostly reported carrier effect established in electrocatalysis is just limited to the support participation in catalysis or the metal-support charge transfer (called as electronic metal-support interaction, namely EMSI) [11–15], seldom altering guest's phase composition and construction.

While among wide scope of carrier effects, the so-called strong metal-support interaction (SMSI) effect proposed by Tauster et al. in late 1970 s can realize the tailoring of guests' phase composition and structure due to its unusual forming conditions and mechanisms [16–18]. Traditionally, this effect often happens in high temperature reduction treatment of noble-metal nanoparticles (NPs) supported on reducible oxides such as CeO_2, TiO_2 and Fe_3O_4 [19–21]. Two phenomena would occur upon SMSI affects[22,23]: (i) the partially reduced metal oxide migrates onto guest metal NPs surface to form an oxide overlayer. This is driven by minimization of high surface energy of metal NPs by mobile substoichiometric oxide species. (ii) a bimetallic alloy generates between the guest metal and the metal component of the support. Obviously, these two interfacial processes lead to two distinct catalyst states and separately rearrange the structure and the composition of supported metal NPs. More importantly, guest metals' electronic structures can be profoundly regulated by the concomitantly induced strong metal-oxide interactions and alloying effects (including strain effect and ligand

---

* Corresponding author.
** Corresponding author at: College of Safety Engineering, Chongqing University of Science & Technology, Chongqing 401331, China.
   E-mail addresses: zxingqun@cqu.edu.cn (X. Zheng), nieyao@cqu.edu.cn (Y. Nie).

effect) [24,25], resulting in significant modulations of catalytic activity, selectivity and stability[17–23].

Despite the intriguing phenomenological effects, the SMSI is extensively applied to enhance modern industrial catalysis and scarcely employed in electrocatalysis [26]. One obstacle might be that the creation of SMSI is usually accompanied by serious sintering of guest metal NPs due to the high-temperature (>500 °C) redox treatment [27,28], which lowers active surface areas for electrocatalysis. Recently proposed methods based on wet-chemistry, ultrafast laser excitation and ball milling can avoid this problem [29–31], but the methodological development for constructing SMSI at low-temperature is still very limited. Moreover, previously SMSI investigations are mainly focused on oxide overlayer formation, whilst the interfacial alloying between the supported metal and the metal component in oxide supports is achieved less frequently as it requires more harsh conditions (much higher temperature or longer reaction time) [32,33]. In that case, only the catalysis architecture is modulated while the phase composition reformation and alloying effects induction cannot be fulfilled due to the missing of SMSI alloying mechanism. Therefore, in order to broaden the application of SMSI in electrocatalysis and fully exploit the superiority of SMSI in refurbishing guest's catalytic configurations, developing a general methodology that can not only create SMSI at relatively low temperature, but also controllably manipulate two specific SMSI mechanisms and easily make them appear together is highly desired, but still unachieved yet.

Herein, a low-temperature solvothermal-induced SMSI covering two specific mechanisms is constructed to simultaneously renovate the phase composition and structure of Pt nanocubes (NCs). Key to the success is to pre-create a doping in the oxide support and establish a redox interaction between the support and the guest metal. Given that the reducible CeO_2 is known to generate SMSI and can be easily doped by heterogeneous Cu^{2+} [34,35], we thereby applied Cu^{2+} doped ceria anchored on carbon substrate ($CeCuO_x/C$, $1.5 < x < 2$) as a typical example to create SMSI with Pt. Specifically, $Pt(acac)_2$ source was firstly adsorbed on $CeCuO_x/C$ and then a 140 °C solvothermal reaction using N, N dimethylformamide (DMF) as both solvent and reductant was performed (Fig. 1). Apart from producing Pt NCs [36], the DMF solvothermal treatment also induced the SMSI effect covering the migration of substoichiometric CeO_x onto the Pt surface and the alloying of Cu^{2+} in the support with guest Pt, endowing the resultant product with surface partially decoration of CeO_x and cubic PtCu alloy phase (denoted as $CeO_x/PtCu/CeCuO_x/C$, Fig. 1). To the best of our knowledge, this is the first report on the low-temperature solvothermal-induced SMSI. The simultaneous emergence of two SMSI mechanisms caused ~0.95 % compressive strain on Pt and aroused strong electronic interactions between Pt, Cu and surrounding CeO_x overlayers, resulting in adjusted valence state of Pt and optimized adsorption energies toward reactive intermediates. Benefiting from those, the $CeO_x/PtCu/CeCuO_x/C$ delivered much strengthened MOR activity, CO tolerance capability and long-term stability in an acid electrolyte, validating the promising role of SMSI in improving the overall MOR electrocatalytic performance.
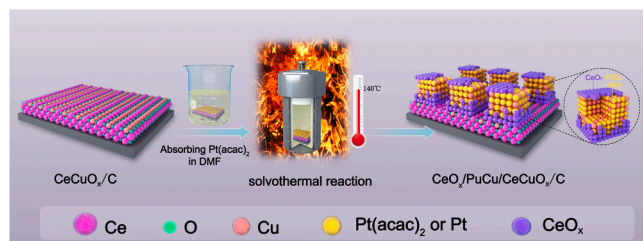

Fig. 1. Schematic illustration of the fabrication process.

2. Materials and methods

2.1. Materials

Platinum acetylacetonate ($Pt(acac)_2$), cerium nitrate hexahydrate ($Ce(NO_3)_3 \cdot 6 H_2O$), copper nitrate trihydrate ($Cu(NO_3)_2 \cdot 3 H_2O$), sodium hydroxide (NaOH), N,N-Dimethylformamide (DMF), sulfuric acid (H_2SO_4) and methanol (CH_3OH) were purchased from Adamas-beta. Commercial Pt/C (20 wt%) was purchased from American Johnson-Matthey Corporation. Carbon black powder (Vulcan XC-72R) was purchased from Cabot Corporation. Nafion (5 wt%) was purchased from Sigma-Aldrich. Deionized water used in the experiments was ultrapure grade and the resistivity is 18 MΩ/cm.

2.2. Synthesis of $CeCuO_x/C$

80 mg Vulcan XC-72 carbon powder was firstly ultrasonically mixed with 40 mL deionized water for around 15 min to obtain a highly homogeneous solution, then 64 μL $Ce(NO_3)_3$ solution (0.8 mol/L) and 64 μL $Cu(NO_3)_2$ solution (0.8 mol/L, so the theoretical Cu^{2+}/Ce^{3+} ratio was controlled at 1:1) were added into the above mixture solution under magnetic stirring. After continuous stirring for 24 h at room temperature, 193.1 mg NaOH dissolved in 10 mL deionized water was slowly dropped into above-mixed solution and the reaction mixture was held stirring for another 12 h. After filtrating, washing and drying, the $CeCuO_x/C$ was obtained.

2.3. Synthesis of $CeO_x/PtCu/CeCuO_x/C$

In a typical synthesis, 80 mg of $CeCuO_x/C$, 40.3 mg of $Pt(acac)_2$ and 70 mL of DMF were added into a 100 mL beaker, followed by vigorous magnetic stirring at room temperature for 24 h. Afterward, the mixture solution was transferred into a 100 mL Teflon-lined stainless-steel autoclave and kept at 140 °C for 22 h. After cooling to room temperature naturally, the suspension was filtered and washed multiple times with 1:1 ethanol/water. After drying at 60 °C in a vacuum oven for 4 h, the $CeO_x/PtCu/CeCuO_x/C$ was obtained.

A counterpart with PtCu NCs directly loading on the carbon substrate (denoted as PtCu/C) was prepared by the similar solvothermal procedure to above except adding mixture of 64 μL $Cu(NO_3)_2$, 40.3 mg Pt $(acac)_2$ and 70 mL DMF into the Teflon-lined stainless-steel autoclave.

3. Results and discussions

3.1. Phase composition and structure characterizations

Transmission electron microscopy (TEM) was initially utilized to characterize the morphology of the resultant $CeO_x/PtCu/CeCuO_x/C$. As shown in Fig. 2a, NPs in $CeO_x/PtCu/CeCuO_x/C$ exhibit cubic-like morphology with average size of 9.91 nm, which is comparable to the size of Pt-based NCs synthesized in other literatures (~10 nm) [37,38]. The TEM of PtCu/C counterpart (PtCu NCs directly loading on carbon substrate) was also characterized and Pt cubes in PtCu/C own an average size of 13.51 nm (Fig. S1). Further high-resolution TEM observations of NCs in $CeO_x/PtCu/CeCuO_x/C$ clearly reveal an interplanar spacing of 0.22 nm (Fig. 2b, c and Fig. S2), which is slightly smaller than that of the standard face-centered cubic (fcc)-structured Pt crystals (0.23 nm), providing a sign of lattice contraction originating from the incorporation of smaller atoms into Pt lattice structure to generate an alloy phase [39]. In our case, both of Ce and Cu atoms seem have possibilities to migrate from support sites into the Pt lattice, which cannot be ascertained herein and needs further characterizations to identify what alloy phase is formed on earth. On the other hand, an irregular thin overlayer is clearly visible on the NCs' surface (Fig. 2b, Fig. S2), and some lattice fringes assigned to (111), (200) or (220) facet of CeO_2 are detected not only in carbon substrate area, but also in NCs area (Fig. 2c,
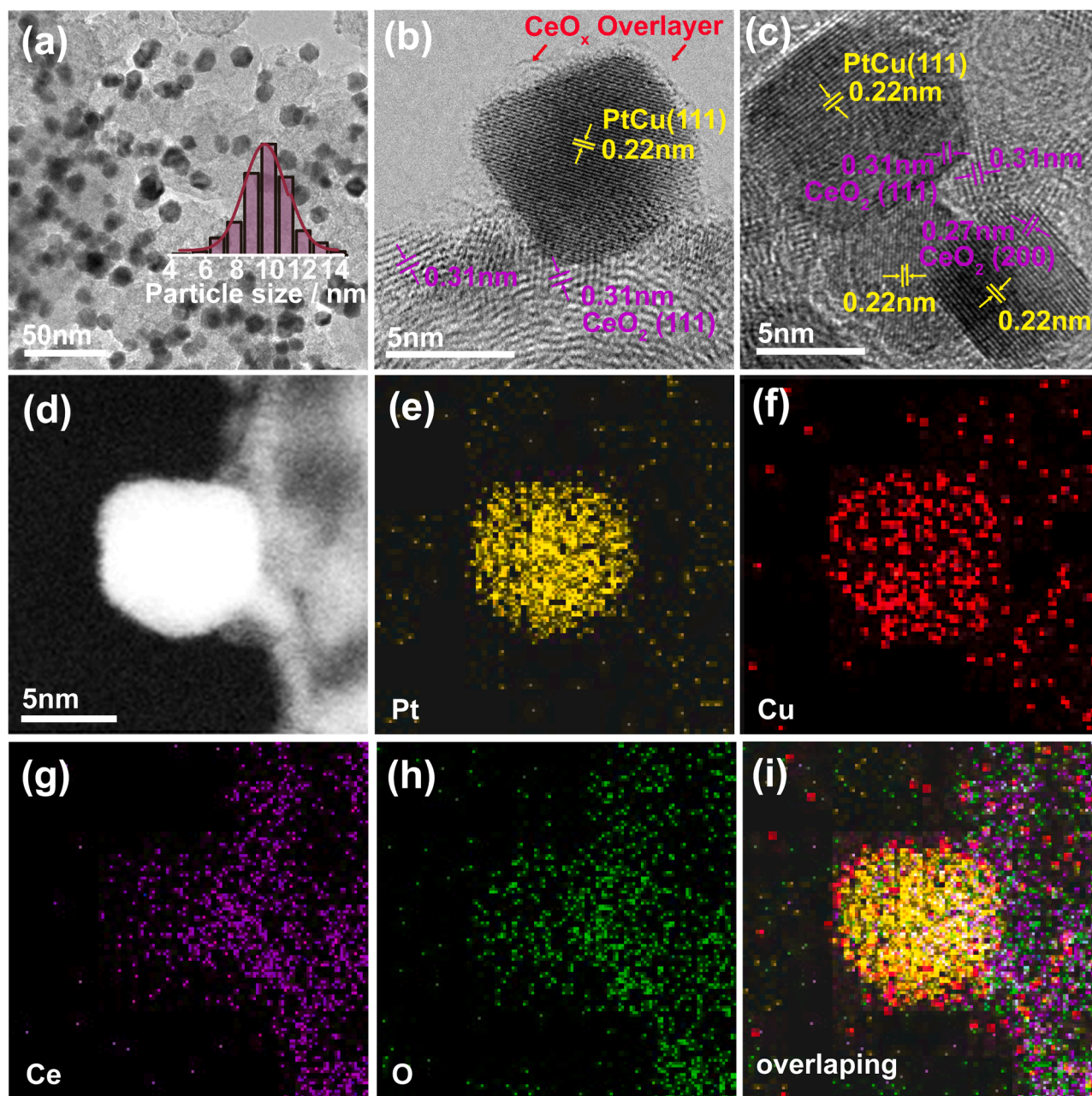
Fig. 2. (a) TEM image of $CeO_x/PtCu/CeCuO_x/C$. (b) and (c) HRTEM image of $CeO_x/PtCu/CeCuO_x/C$. (d) HAADF-STEM image of $CeO_x/PtCu/CeCuO_x/C$ and (e-i) corresponding EDS elemental mapping.

Fig. S2), indicating that an overcoating of the cerium oxide would be formed on NCs' surface due to the solvothermal-induced SMSI oxide migration mechanism.

To clarify the microscopic constructions and phase composition profiles of $CeO_x/PtCu/CeCuO_x/C$ more precisely, the aberration-corrected high-angle annular dark-field scanning transmission electron microscopy (HAADF-STEM) in combination with energy-dispersive X-ray spectroscopy (EDS) were performed, as shown in Fig. 2d-i. For Cu element, a small part disperses on the support area, while the majority distributes homogeneously in where the Pt particle locates and presents a similar size to that of the Pt element, significantly evidencing that Cu has diffused from the support into the Pt phase to generate a PtCu alloy phase during solvothermal process. With regard to the Ce and O elements, they show the same distribution. Considering that if Ce element migrated into Pt lattice to form a PtCe alloy, the Ce element must stay in both PtCe alloy phase and cerium oxide phase, thus the distribution of

Ce element in EDS mapping must be different from that of O element. While the appositional distribution of Ce and O in our case suggests that Ce element only exist in the form of cerium oxide (the XPS and XRD results discussed below can.

also confirm this), preliminary excluding the formation possibility of PtCe alloy [30,32]. Therefore, the interplanar spacing of 0.22 nm detected in Fig. 2b, c and Fig. S2 could be assigned to the (111) planes of face-centered cubic (fcc)-phased PtCu alloy. It is also observed that Ce and O elements disperse on both surface of PtCu cube and carbon substrate, forcefully affirming that the PtCu NCs are partially overcoated by the cerium oxides coming from the pristine $CeCuO_x/C$ support. Above results can primarily determine that a solvothermal-induced SMSI was successfully constructed in the interface between Pt and $CeCuO_x$, and the cerium oxide migration occurs accompanying with the alloying of Cu^{2+} in the support and guest Pt. The actual elements content in $CeO_x/PtCu/CeCuO_x/C$ was determined by inductively coupled plasma

mass spectrometry (ICP-MS), which is listed in Table S1.

Powder X-ray diffraction (XRD) and X-ray photoelectron spectra (XPS) analysis of the $CeO_x/PtCu/CeCuO_x/C$ and the corresponding $CeCuO_x/C$ support were then conducted to explore the variation of chemical compositions and valence states before and after solvothermal reaction. As shown in Fig. 3a, characteristic crystalline peaks associated to the fluorite-structured CeO_2 (JCPDS: 34-0394) are observed in $CeCuO_x/C$ support, indicating the CeO_2 was successfully anchored onto carbon substrate. While there is no presence of any diffraction peaks associated with metallic Cu (JCPDS: 04-0836) or CuO phase (JCPDS: 44-0706) in $CeCuO_x/C$, implying that Cu species may exist primarily in the form of amorphous state in CeO_2 [35,40]. XPS characterization of $CeCuO_x/C$ detected the Cu element (Fig. S3, Table S2) and the analysis of Cu 2p peak of $CeCuO_x/C$ indicates that the copper is mainly in the divalent state (Fig. 3b, Table S3). After solvothermal reaction, diffraction peaks located around 40.1°, 46.6° and 68.0° appear in the XRD pattern of $CeO_x/PtCu/CeCuO_x/C$. As these diffraction peaks locate between those of the standard Pt (JCPDS 04-0802) and Cu (JCPDS 04-0836) references and neither individual Pt nor Cu diffraction peaks are detected, they can be readily corresponding to the (111), (200), and (220) planes of fcc-structured PtCu alloy. This finding further suggests the successful formation of PtCu alloyed phase. The lattice contraction extent of Pt in $CeO_x/PtCu/CeCuO_x/C$ relative to standard pure Pt crystal is 0.95 % (Table S4), as calculated based on Debye-Scherrer equation [41,42]. Such a compressive strain is very desirable as it can downshift the d-band center of Pt, consequently weakening the binding energy towards intermediates and facilitating the catalytic proceedings [43–45]. Characteristic peaks of Cu oxides are also not observed in XRD

pattern of $CeO_x/PtCu/CeCuO_x/C$, and the Cu 2p peak analysis suggests that the amount of metallic Cu in $CeO_x/PtCu/CeCuO_x/C$ increases as compared to that of $CeCuO_x/C$ (Fig. 3b, Table S3). It is noteworthy that the diffraction intensities of CeO_2 in the XRD pattern of $CeO_x/PtCu/-CeCuO_x/C$ are weakened when compared to those of $CeCuO_x/C$ support, which can be due to the redox between guest Pt and host CeO_2.

during solvothermal reaction [46,47]. Such a redox interaction would be the prerequisite for evoking the interfacial oxide migration mechanism of SMSI effect, as the reduction of CeO_2 would let oxygen atoms escape from the lattice and lead to the formation of metastable suboxides [31,48,49]. The partially reduced CeO_2 can be further certified by the increased percentage of Ce^{3+} in $CeO_x/PtCu/CeCuO_x/C$ relative to that in $CeCuO_x/C$ support, as estimated from their Ce 3d peaks analysis (Fig. 3c, Table S5). In addition, the alloying between Pt and Ce atoms can be strongly eliminated again according to XRD and XPS results, as the $CeO_x/PtCu/CeCuO_x/C$ exhibits no CePt alloy phase (JCPDS:19-0295) in XRD pattern (Fig. 3a) and no characteristic peaks related to metallic Ce in Ce 3d spectrum(Fig. 3c) [30,50]. Fig. 3d presents the high-resolution Pt 4 f spectra of $CeO_x/PtCu/CeCuO_x/C$ and PtCu/C counterpart. It can be seen that the Pt 4 f binding energy of $CeO_x/PtCu/CeCuO_x/C$ exhibits an appreciable positive shift of ~0.26 eV with respect to that of PtCu/C, implying an electronic structure alteration of Pt caused by the strong interaction between PtCu and surrounding cerium oxide. This positively shift would also result in a moderated binding strength of intermediate species and benefit the acceleration of reaction process [47,51]. Furthermore, the quantitative analysis shown in Table S6 indicates that $CeO_x/PtCu/CeCuO_x/C$ has a higher atomic ratio of Pt^{2+}/Pt^0 (1.70) than PtCu/C (1.48), which would
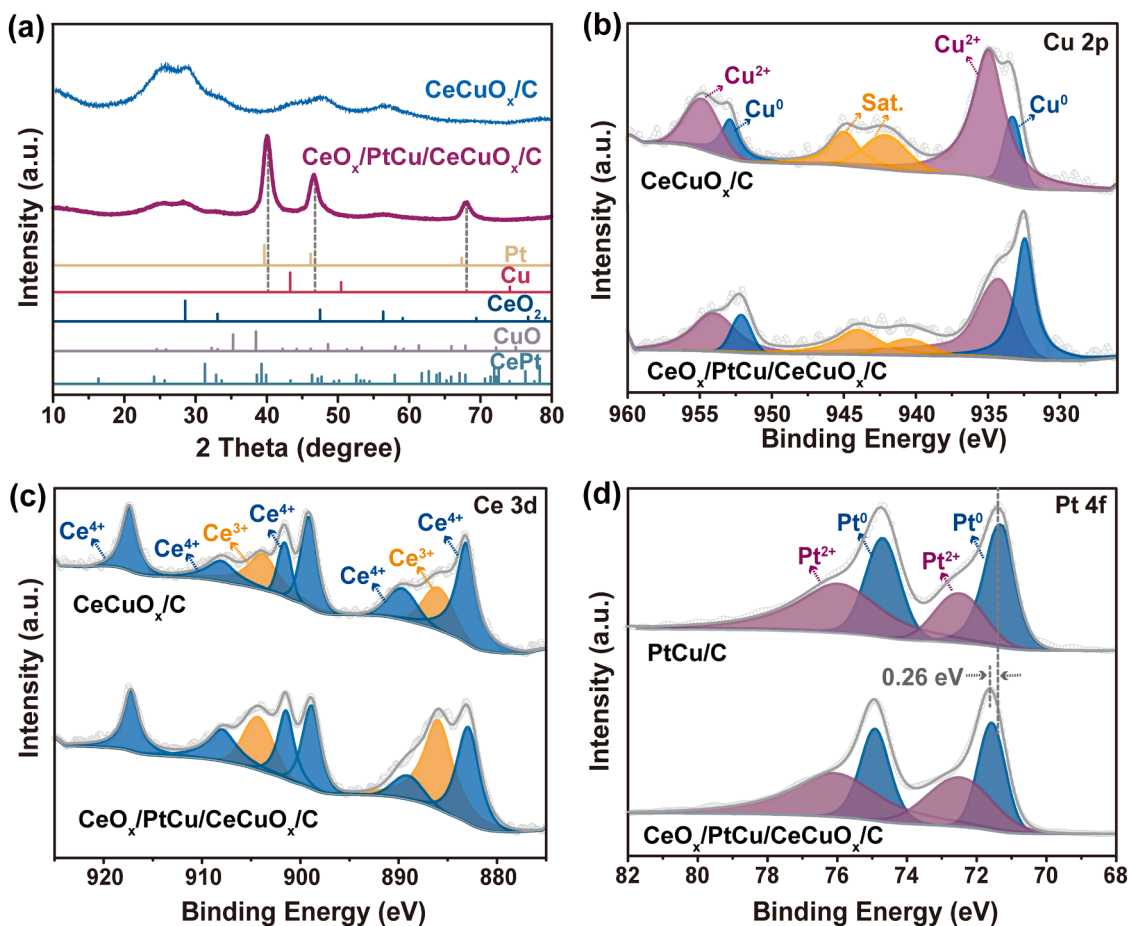
Fig. 3. (a) XRD diffraction patterns of $CeCuO_x/C$ support and $CeO_x/PtCu/CeCuO_x/C$ product (Pt: PDF card #04-0802, Cu: PDF card #04-0836, CeO_2: PDF card #34-0394, CuO: PDF card #44-0706 and CePt: PDF card #19-0295). High-resolution (b) Cu 2p XPS spectra (c) Ce 3d XPS spectra of $CeO_x/PtCu/CeCuO_x/C$ and $CeCuO_x/C$. (d) High-resolution Pt 4 f XPS spectra of $CeO_x/PtCu/CeCuO_x/C$ and PtCu/C.

favor for a high mass/specific MOR activity as demonstrated by previously reports [52,53]. The detailed electronic structure and the specific electron transfer directions in $CeO_x/PtCu/CeCuO_x/C$ were deeply studied by density functional theory (DFT) calculations, which will be discussed later.

3.2. SMSI generation mechanism discussions

On the basic of above analysis, the origin of the solvothermal-induced SMSI oxide migration mechanism can be explained, which is similar to that of the traditional SMSI constructed by high temperature reduction treatment. That is, high-pressure DMF solvothermal treatment of reducible CeO_2 in presence of noble Pt metal induces a redox interaction between Pt and CeO_2, which leads to the formation of partially reduced CeO_x (Fig. 4a, c). As the CeO_x is metastable and the surface tension of Pt is larger than that of CeO_x, the CeO_x tends to move onto the surface of Pt NCs to minimize the surface energy [30]. To elucidate the role of Cu^{2+} dopants in oxide migration process, the contrast sample with $Pt(acac)_2$ absorbed on Cu^{2+} un-doped CeO_2/C was subjected into the similar solvothermal procedure and the obtained sample was denoted as $CeO_x/Pt/CeO_2/C$ (its TEM image is shown in Fig. S4). HAADF-STEM and EDS profiles of $CeO_x/Pt/CeO_2/C$ shown in Fig. S5 directly indicate that a similar overlayers of cerium oxides is formed on pure Pt NCs, verifying that the CeO_x migration process is independent from Cu^{2+} dopants in our case and can generally occur as long as the Pt and reducible CeO_2 is coexisted under solvothermal reduction condition.

With regard to the alloying mechanism happening between Cu^{2+} in the support and guest Pt, it could be mainly ascribed to the easy mobility and large reduction tendency of Cu^{2+} under high pressure solvothermal condition. To manifest it, we directly subjected the $CeCuO_x/C$ support into the same solvothermal reaction and the obtained sample was denoted as $CeCuO_x/C$-st. The XRD of $CeCuO_x/C$-st shown in Fig. S6 presents apparent diffraction peaks assigned to the metallic Cu phase, demonstrating that the pre-doped Cu^{2+} in $CeCuO_x/C$ has large reduction tendency during solvothermal process (Fig. 4b, c). While given the XRD pattern of $CeO_x/PtCu/CeCuO_x/C$ shown in Fig. 3a shows no characteristic peaks of metallic Cu, it can be rationally speculated that the

reduction of Cu^{2+} was accompanying with its diffusion into Pt lattice during solvothermal treatment, thus resulting in the generation of PtCu alloyed phase in $CeO_x/PtCu/CeCuO_x/C$ (Fig. 4c). Moreover, such an alloying of Cu^{2+} in the support with guest Pt can be achieved over a wide range of pre-doped Cu^{2+} content, as evidenced by the XRD, HRTEM, HAADF-STEM and EDS mapping results (Figs. S7-S9) of other two $CeO_x/PtCu/CeCuO_x/C$-0.2 and $CeO_x/PtCu/CeCuO_x/C$-1.5 samples (where the 0.2 and 1.5 represent the feeding Cu^{2+}/Ce^{3+} ratio). These results validate that the alloying mechanism of SMSI can be easily induced by solvothermally reducing Pt source in presence of Cu^{2+} pre-doped CeO_2.

3.3. MOR performance evaluations

After understanding the composition, structure and formation mechanism of $CeO_x/PtCu/CeCuO_x/C$, its electrocatalytic properties toward methanol oxidation were probed. To investigate the effect of SMSI, reference samples including PtCu/C, $CeO_x/Pt/CeO_2/C$ and commercial Pt/C were also appraised under the identical test condition. Fig. 5a shows the cyclic voltammograms (CVs) performed in N_2-saturated 0.5 M H_2SO_4 electrolyte with a sweep rate of 50 mV s^{-1}. All catalysts exhibit well-defined peaks assigned to hydrogen adsorption/desorption in the potential region of 0.05–0.4 V. Through measuring the Coulombic charge for hydrogen adsorption and desorption, the electrochemical surface area (ECSA) of $CeO_x/PtCu/CeCuO_x/C$, PtCu/C, $CeO_x/Pt/CeO_2/C$ and commercial Pt/C is calculated to be 36.3 m^2 g^{-1}, 31.1 m^2 g^{-1}, 33.4 m^2 g^{-1} and 66.5 m^2 g^{-1}, respectively. The smaller ECSA value of $CeO_x/PtCu/CeCuO_x/C$, PtCu/C and $CeO_x/Pt/CeO_2/C$ compared to commercial Pt/C is owing to the larger size of PtCu or Pt NCs [38,54]. Moreover, the asterisk-marked peaks located around 0.22 V vs. RHE in CV curves of $CeO_x/PtCu/CeCuO_x/C$, PtCu/C and $CeO_x/Pt/CeO_2/C$ are identified as the H adsorption/desorption features of single crystal Pt (100) [38,55], further revealing the cubic shape of Pt in these catalysts.

Fig. 5b presents the CV curves of the studied catalysts recorded in 0.5 M H_2SO_4 + 0.5 M CH_3OH. Apparently, the $CeO_x/PtCu/CeCuO_x/C$ catalyst displays the lowest onset oxidation potential (0.448 V vs. RHE) and the strongest peak current (4.54 mA cm^{-2}) in the forward peak as compared with PtCu/C (0.541 V vs. RHE, 3.61 mA cm^{-2}), $CeO_x/Pt/$
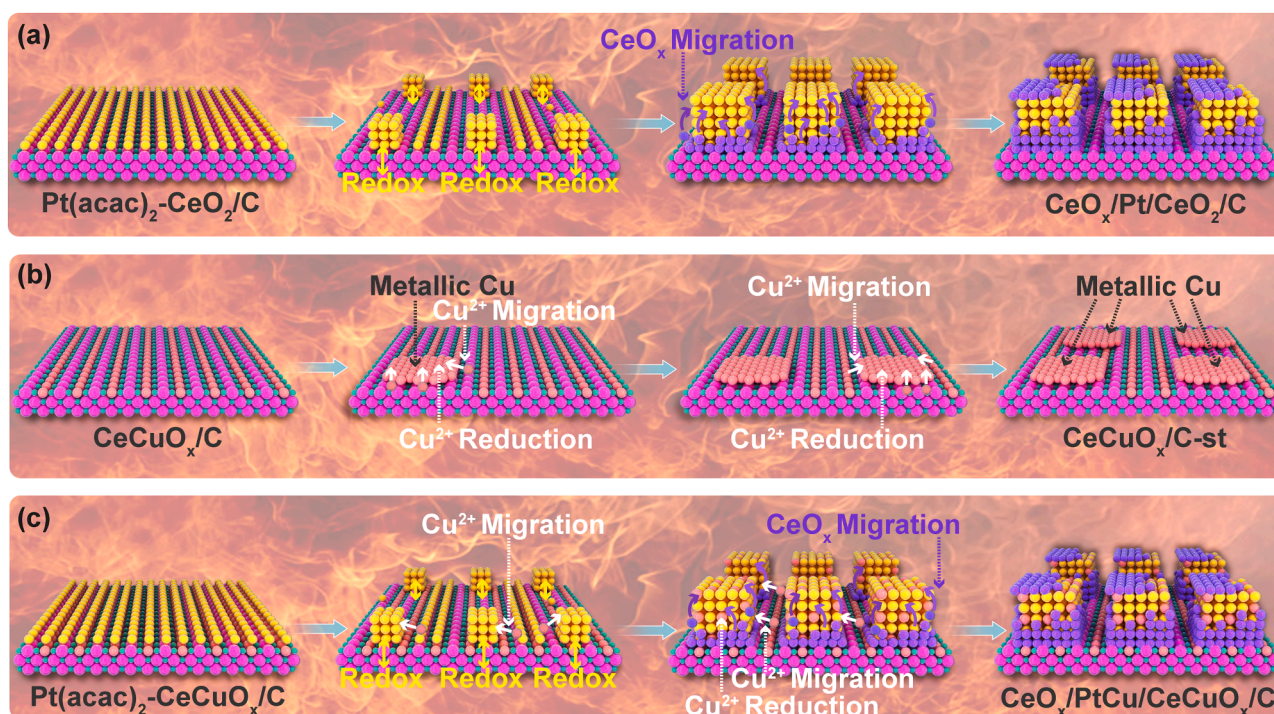
Fig. 4. Phase composition and structure evolutions of (a) $CeO_x/Pt/CeO_2/C$, (b) $CeCuO_x/C$-st and (c) $CeO_x/PtCu/CeCuO_x/C$ during solvothermal treatment.
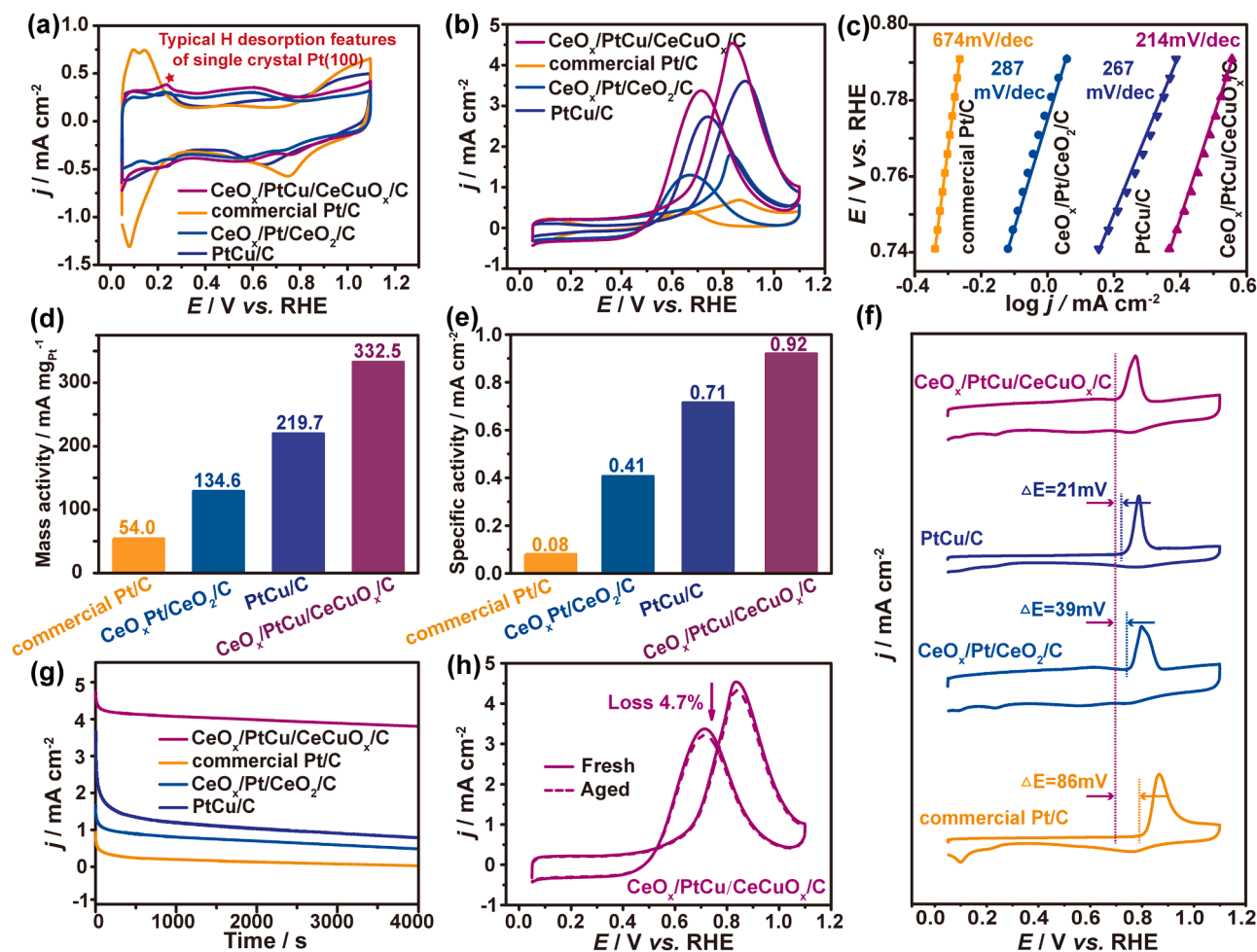
Fig. 5. (a) CVs for catalysts measured in 0.5 M H$_2$SO$_4$ solutions. (b) CVs for catalysts measured in 0.5 M H$_2$SO$_4$ + 0.5 M CH$_3$OH solutions. (c) Tafel plots. (d) Comparisons of mass activity for four catalysts. (e) Comparisons of specific activity for four catalysts. (f) CO stripping voltammograms for catalysts. (g) Chronoamperometric curves of tested catalysts measured at the fixed potential of 0.8 V vs. RHE. (h) CV curves of MOR before and after 600 cycles stability test for CeO$_x$/PtCu/CeCuO$_x$/C.

CeO$_2$/C (0.615 V vs. RHE, 1.79 mA cm^{-2}) and commercial Pt/C (0.636 V vs. RHE, 0.69 mA cm^{-2}), indicating that the CeO$_x$/PtCu/CeCuO$_x$/C possesses the highest MOR activity among these catalysts. The better activity of CeO$_x$/PtCu/CeCuO$_x$/C relative to non-SMSI affected PtCu/C and commercial Pt/C preliminarily highlights the.

superiority of SMSI in enhancing the inherent MOR activity, while the much inferior activity of CeO$_x$/Pt/CeO$_2$/C compared to CeO$_x$/PtCu/CeCuO$_x$/C and PtCu/C reflects the importance of PtCu alloy synergy induced by the SMSI alloying mechanism. The Tafel plots derived from the MOR CV curves were then provided to evaluate the catalytic kinetics of tested electrocatalysts. As shown in Fig. 5c, the CeO$_x$/PtCu/CeCuO$_x$/C shows a Tafel slope of 214 mV per decade, lower than that of PtCu/C (267 mV/dec), CeO$_x$/Pt/CeO$_2$/C (287 mV/dec) and commercial Pt/C (674 mV/dec), suggesting a more favorable MOR catalytic kinetics of CeO$_x$/PtCu/CeCuO$_x$/C [56]. To gain deeper insights into the activity of catalysts, the peak current at 0.85 V vs. RHE associated with MOR in the forward scan was normalized to both ECSA and the loading amount of metal Pt. As illustrated in Fig. 5d, the mass activity of CeO$_x$/PtCu/Ce-CuO$_x$/C is calculated to be 332.5 mA mg$_{Pt}^{-1}$, which is 1.51, 2.47 and 6.16 times greater than that of PtCu/C (219.7 mA mg$_{Pt}^{-1}$), CeO$_x$/Pt/CeO$_2$/C (134.6 mA mg$_{Pt}^{-1}$) and commercial Pt/C (54.0 mA mg$_{Pt}^{-1}$), respectively. Given that the CeO$_x$/PtCu/CeCuO$_x$/C has a smaller ECSA than commercial Pt/C, the higher mass activity of CeO$_x$/PtCu/CeCuO$_x$/C can be rationally attributed to the inherently enhanced activity of active sites [57,58]. The specific activity of CeO$_x$/PtCu/CeCuO$_x$/C achieves a value

of 0.92 mA cm^{-2} (Fig. 5e), exceeding those of PtCu/C (0.71 mA cm^{-2}), CeO$_x$/Pt/CeO$_2$/C (0.41 mA cm^{-2}) and commercial Pt/C (0.08 mA cm^{-2}) by 1.30, 2.24 and 11.50 times, respectively. Meanwhile, the MOR electrocatalytic activity of CeO$_x$/PtCu/CeCuO$_x$/C is superior or comparable to many previous reported Pt-based MOR catalysts in acidic electrolytes, as briefly listed in Table S7.

The CO-stripping experiment was applied to assess the anti-poisoning ability of adsorbed CO intermediates. As depicted in Fig. 5f, the onset potential of CO oxidation (Table S8) for the CeO$_x$/PtCu/CeCuO$_x$/C negatively shift by 21, 39 and 86 mV with respect to those of PtCu/C, CeO$_x$/Pt/CeO$_2$/C and commercial Pt/C, respectively. This reveals that the CO can be more easily oxidized and removed from the surface of CeO$_x$/PtCu/CeCuO$_x$/C, signifying that the CeO$_x$/PtCu/CeCuO$_x$/C possesses a stronger resistance to CO poisoning. The tolerance capability to the toxic CO can be also reflected by the peak current density ratio of the forward-to-backward scans (I$_f$/I$_b$). As listed in Table S8, the I$_f$/I$_b$ of the CeO$_x$/PtCu/CeCuO$_x$/C is 1.37, larger than that of PtCu/C (1.34), CeO$_x$/Pt/CeO$_2$/C (1.33) and commercial Pt/C (1.30), further manifesting the stronger anti-poisoning ability to CO of CeO$_x$/PtCu/CeCuO$_x$/C.

Regarding the catalysts' durability for MOR, chronoamperometric (CA) measurements were firstly conducted at 0.8 V vs. RHE in 0.5 M H$_2$SO$_4$ + 0.5 M CH$_3$OH electrolyte. As displayed in Fig. 5g, the CeO$_x$/PtCu/CeCuO$_x$/C catalyst shows an obviously slower current density decay and maintains much higher current density after 4000 s test

relative to other catalysts, demonstrating a much strengthened stability of CeO$_x$/PtCu/CeCuO$_x$/C. CV scanning tests were also employed to evaluate the stability. As shown in Fig. 5h, the CeO$_x$/PtCu/CeCuO$_x$/C only shows 4.7 % decay after 600 sequential cycles, much better than that of PtCu/C (59 %, Fig. S10a), CeO$_x$/Pt/CeO$_2$/C (11 %, Fig. S10b) and commercial Pt/C (44 %, Fig. S10c), further evidencing an enhanced stability of CeO$_x$/PtCu/CeCuO$_x$/C. TEM image of CeO$_x$/PtCu/CeCuO$_x$/C after the CA test shows no obvious changes in the morphology, particle size and distribution (Fig. S11), supporting the robust durability. Whilst, the PtCu/C (Fig. S12) and commercial Pt/C (Fig. S13) exhibit apparent particle agglomeration and size increase after the CA stability test. These findings significantly highlight that the cerium oxide overcoatings in CeO$_x$/PtCu/CeCuO$_x$/C can stabilize the particles and prevent them from severe coalescence, which is accordance with previous SMSI studying [29,59]. Combined together, the above findings collectively demonstrate that the partial surface decoration of cerium oxide and the alloying of Cu with Pt leads to a dual increase in catalytic activity and stability, holding great promises as an efficient catalyst for liquid-fuel electrooxidations.

3.4. Theoretical calculations

To reveal the origin of the enhanced MOR electrocatalytic performance on CeO$_x$/PtCu/CeCuO$_x$/C, DFT calculations were implemented. Four surfaces including CeO$_x$/PtCu(100)/CeCuO$_x$, PtCu(100), CeO$_x$/Pt(100)/CeO$_2$ and Pt(100) were modeled (Fig. S14). Fig. S15 displays the charge density difference and Bader charge of pure Pt(100) and PtCu (100). Their comparison suggests that replacing Pt with Cu atoms would induce a net charge of 0.44e$^-$ transferring from Cu to Pt. When the surficial CeO$_x$ clusters and the CeCuO$_x$ substrate present, such an electronic transfer from Cu to Pt becomes more apparent (0.52e$^-$) in the CeO$_x$/PtCu(100)/CeCuO$_x$ (Fig. S16). Moreover, the CeO$_x$/PtCu(100)/CeCuO$_x$ also has a charge of 1.08e$^-$ transferring from PtCu(100)/CeCuO$_x$ to CeO$_x$ clusters (Fig. 6a), which can be ascribed to the more electronegative O in CeO$_x$. A similar electronic transfer from Pt(100)/CeO$_2$ to CeO$_x$ is observed in CeO$_x$/Pt(100)/CeO$_2$ (0.52e$^-$, Fig. S17), but it is much

weaker than that in CeO$_x$/PtCu(100)/CeCuO$_x$ case. From above, it can be preliminarily concluded that there exist two electron transfer processes in CeO$_x$/PtCu(100)/CeCuO$_x$, i.e., the Cu in PtCu(100) donates electrons for Pt, and the CeO$_x$ overlayer withdraws electrons from Pt. As the electron transportation from Pt to surficial CeO$_x$ clusters (1.08e$^-$) is much stronger than that from Cu to Pt (0.52e$^-$), the Pt atoms locating at CeO$_x$/PtCu(100)/CeCuO$_x$ interface are under electron deficient state, corroborating the XPS result. These strong interactions within CeO$_x$/PtCu(100)/CeCuO$_x$ collaboratively induce a downward shift of d-band center of Pt (Table S9), which would lead to a weakened binding strength toward reaction-involved intermediates [60,61].

Then the free energy changes during the CO poisoning pathway of MOR (i.e., CH$_3$OH→*CH$_2$OH→*CHOH→*COH→*CO→*CO+*OH→CO$_2$) on four modeled surfaces were calculated. As shown in Fig. 6b, the co-adsorption of *CO+ *OH and the conversion from *CO+ *OH to CO$_2$ are the key reaction steps for all surfaces as these two steps meet relative large energy costs. While the energy barriers of these two steps on CeO$_x$/PtCu (100)/CeCuO$_x$ (0.50 eV and 0.48 eV, respectively) are much lower than those on other three catalyst models, indicating a stronger reaction trend on CeO$_x$/PtCu(100)/CeCuO$_x$. For the *CO formation step, the CeO$_x$/PtCu (100)/CeCuO$_x$ shows the smallest energy release (0.59 eV) than other catalysts, meaning that the CeO$_x$/PtCu(100)/CeCuO$_x$ has the lowest possibility to be poisoned by *CO, which well supports the experimental results. To explain this, we further calculated the absorption energy of *OH (ΔE_{OH}) and *CO (ΔE_{CO}), two key descriptors for the MOR, on four above-mentioned models and another PtCu(100)/CeCuO$_x$ counterpart model (Fig. S18). Catalysts with excellent MOR performances usually exhibit a strong adsorption of OH and a weak adsorption of CO [5,6,41,43]. As shown in Fig. 6c and Table S9, the CeO$_x$/PtCu(100)/CeCuO$_x$ shows the weakest ΔE_{CO} among all modeled surfaces, suggesting the easiest desorption of the toxic *CO intermediate on CeO$_x$/PtCu(100)/CeCuO$_x$, which is in accordance with electrochemical results. Moreover, the CeO$_x$/PtCu (100)/CeCuO$_x$, as well as the PtCu(100)/CeCuO$_x$ and the PtCu(100), have weaker adsorption energies for both *CO and *OH as compared to non-alloyed CeO$_x$/Pt(100)/CeO$_2$ and Pt(100) surfaces, agreeing well with above-mentioned assertions that alloying Pt with smaller Cu atoms can
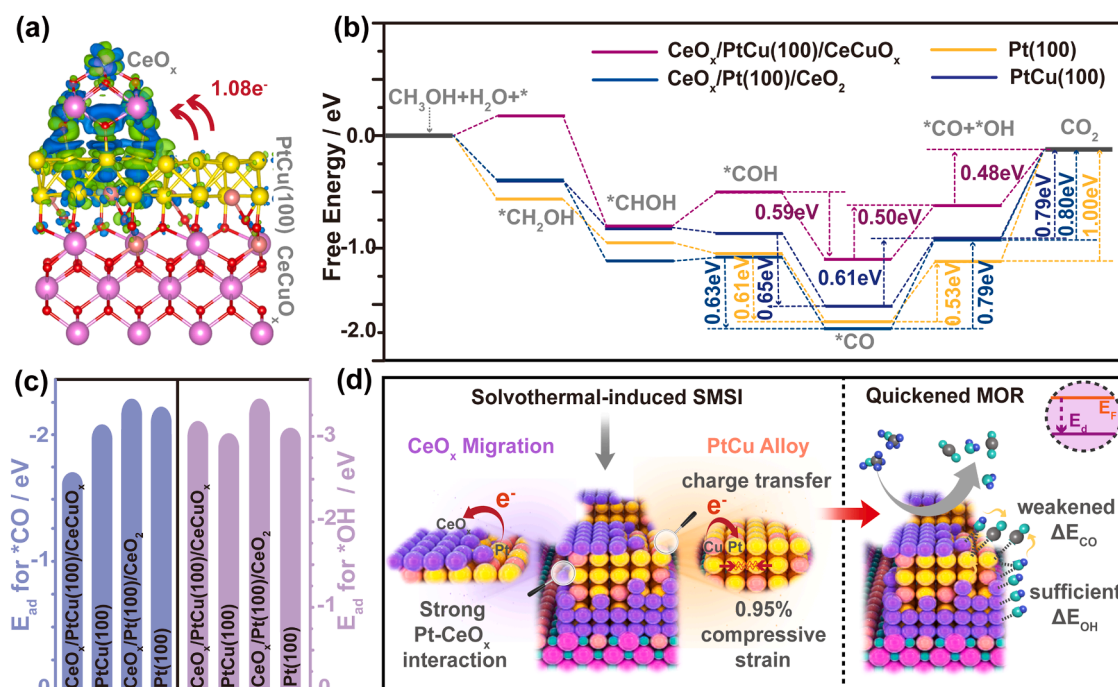
Fig. 6. (a) The 3D charge density difference of modeled CeO$_x$/PtCu(100)/CeCuO$_x$ surface. The blue and green isosurfaces represent charge accumulation and depletion, respectively, with isosurface level set to 0.002e Å^{-3}. (b) The free energy diagram of MOR on modeled surfaces. (c) Adsorption energy (E$_{ad}$) of *CO and *OH of modeled surfaces. (d) Schematic illustration of structure-performance-mechanism relationship.

attenuate the binding strength of intermediates due to the induced compressive strain effect [62,63]. With regard to $CeO_x/PtCu(100)/CeCuO_x$ and $PtCu(100)$, the former one exhibits a weaker ΔE_{CO} than the later one, which can be ascribed to the much lower d-band center position of $CeO_x/PtCu(100)/CeCuO_x$ (Table S9). While the ΔE_{OH} of $CeO_x/PtCu(100)/CeCuO_x$ is slightly higher than that of $PtCu(100)$, indicating that the Pt in $CeO_x/PtCu(100)/CeCuO_x$ binds *OH more easily. This can be due to the presence of unsaturated coordinated Ce atoms (namely, Ce^{3+}) located at the interface between CeO_x and $PtCu(100)$, which exhibit inherently strong affinity to oxygen-containing species as widely indicated by previously literatures[64,65]. In our case, we also found that the oxygen in *OH tends to simultaneously bond with interfacial Pt and Ce atoms (Fig. S19), which would be very beneficial for MOR as the *OH can serves as the oxidant to remove the *CO on adjacent Pt sites by oxidizing *CO to CO_2. This thereby explains why the free energies of *CO+ *OH co-adsorption and CO_2 formation steps are much reduced on $CeO_x/PtCu(100)/CeCuO_x$. It should be pointed out that the only existence of $CeCuO_x$ substrate can also enhance the adsorption of *OH, as demonstrated by the stronger ΔE_{OH} of $PtCu(100)/CeCuO_x$ than that of $PtCu(100)$ (Fig. 6c, Table S9). Further comparison of adsorption energy values of $CeO_x/PtCu(100)/CeCuO_x$ and $PtCu(100)/CeCuO_x$ reveals that they have comparable ΔE_{OH}, but the former one owns the weaker ΔE_{CO} and the lower d-band center (Table S9), suggesting that the extra presence of surficial CeO_x could farther alter the Pt electronic structure and weaken the *CO binding strength due to the strong electronic interaction between Pt and CeO_x overlayers. The presence of cerium oxide can remarkably enhance *OH adsorption can be further confirmed by the strongest ΔE_{OH} showed by $CeO_x/Pt(100)/CeO_2$. Despite that, $CeO_x/Pt(100)/CeO_2$ binds *CO too strong due to the lack of alloying effect, thus its anti-CO poisoning capability and MOR activity are very limited as revealed by the electrochemical results.

By combining DFT calculations with above physical and electrochemical results, the possible mechanism of enhanced MOR electrocatalytic activities can be proposed. As illustrated in Fig. 6d, the solvothermal-induced SMSI results in the formation of PtCu alloyed phase and CeO_x overlayer, simultaneously generating the compressive strain effect, ligand effect (charge transfer from Cu to Pt) and strong Pt-CeO_x interaction. The coupling of these effects and electronic interactions endows the Pt in $CeO_x/PtCu/CeCuO_x/C$ with more electron-deficient features and a downshifted d-band center, thereby intrinsically weakening the *CO adsorption energy and effectively enhance the activity and anti-poisoning ability for MOR. At another level, the CeO_x strengthens *OH adsorption at $CeO_x/PtCu/CeCuO_x/C$ interface, further speeding up the oxidation and removal of *CO blocked at the Pt sites. Therefore, the SMSI-influenced architectural superiorities, the induced alloying effects and strong metal-oxide interactions synergistically contribute to an obviously promoted methanol electrooxidation process on $CeO_x/PtCu/CeCuO_x/C$, well explaining the results detected experimentally.

4. Conclusions

In summary, a strong metal-support interaction covering oxide migration and alloying mechanisms has been successfully created in the Cu^{2+}-doped cerium oxide supported Pt system via a low-temperature solvothermal strategy. The induced two specific SMSI mechanisms were evidenced by partial coverage of supported NCs with CeO_x overlayer and formation of bimetallic PtCu alloy, which largely remodel the catalysis configurations of loaded Pt. The resultant $CeO_x/PtCu/CeCuO_x/C$ exhibited much improved MOR activity and stability than non-SMSI affected or individual CeO_x covered counterparts in an acid electrolyte. The underlying reasons revealed by physical and theoretical studies showed 0.95 % compressive strain, apparent Pt-Cu electronic interactions and strong Pt-CeO_x interactions in $CeO_x/PtCu/CeCuO_x/C$, finally resulting in an electron-deficient state of Pt and modified adsorption energies toward reactive intermediates. This solvothermal-induced SMSI could be extended to a range of noble metal/

heteroatom-doped reducible oxides systems, providing a new design strategy for regulating the catalytic activity and stability of supported electrocatalysts.

CRediT authorship contribution statement

Yi Wang (2021110512041@stu.cqnu.edu.cn)**:** preparing catalysts; Writing – original draft. **Xingqun Zheng:** conducting theoretical calculation, data analysis; Writing – review & editing. **Zhaohong Li, Jianfeng Song, Yulin Chen, Xinzhe Cao:** They helped to prepare catalysts and do the repetitive experiments. **Rui Wu** and **Yi Wang** (ywang@cqnu.edu.cn)**:** providing server for catalyst characterizations; providing constructive suggestions. **Yao Nie:** designing the idea and experiment; data analysis; revising original draft; Writing – review & editing; Funding acquisition.

Declaration of Competing Interest

The authors declare that they have no known competing financial interests or personal relationships that could have appeared to influence the work reported in this paper.

Data availability

No data was used for the research described in the article.

Acknowledgements

Appendix A. Supporting information

Supplementary data associated with this article can be found in the online version at doi:10.1016/j.apcatb.2023.122383.

References

[1] F. Kong, X. Liu, Y. Song, Z. Qian, J. Li, L. Zhang, G. Yin, J. Wang, D. Su, X. Sun, Selectively coupling Ru single atoms to PtNi concavities for high-performance methanol oxidation via d-band center regulation, Angew. Chem. Int. Ed. 61 (2022) e202207524.

[2] Z. Jiang, M. Jing, X. Feng, J. Xiong, C. He, M. Douthwaite, L. Zheng, W. Song, J. Liu, Z. Qu, Stabilizing platinum atoms on CeO_2 oxygen vacancies by metal-support interaction induced interface distortion: mechanism and application, Appl. Catal. B Environ. 278 (2020), 119304.

[3] Y. Chen, J. Pei, Z. Chen, A. Li, S. Ji, H. Rong, Q. Xu, T. Wang, A. Zhang, H. Tang, J. Zhu, X. Han, Z. Zhuang, G. Zhou, D. Wang, Pt atomic layers with tensile strain and rich defects boost ethanol electrooxidation, Nano Lett. 22 (2022) 7563–7571.

[4] L. Hui, X. Zhang, Y. Xue, X. Chen, Y. Fang, C. Xing, Y. Liu, X. Zheng, Y. Du, C. Zhang, F. He, Y. Li, Highly dispersed platinum chlorine atoms anchored on gold quantum dots for a highly efficient electrocatalyst, J. Am. Chem. Soc. 144 (2022) 1921–1928.

[5] M. Qiao, F. Meng, H. Wu, Y. Wei, X. Zeng, J. Wang, PtCuRu nanoflowers with Ru-rich edge for efficient fuel-cell electrocatalysis, Small 18 (2022) 2204720.

[6] K. Zhang, J. Qiu, J. Wu, Y. Deng, Y. Wu, L. Yan, Morphological tuning engineering of Pt@TiO_2/graphene catalysts with optimal active surfaces of support for boosting catalytic performance for methanol oxidation, J. Mater. Chem. A 10 (2022) 4254–4265.

[7] W. Li, L. Zhao, X. Jiang, Z. Chen, Y. Zhang, S. Wang, Confinement engineering of electrocatalyst surfaces and interfaces, Adv. Funct. Mater. 32 (2022) 2207727.

[8] J. Park, S. Lee, H.E. Kim, A. Cho, S. Kim, Y. Ye, J.W. Han, H. Lee, J.H. Jang, J. Lee, Investigation of the support effect in atomically dispersed Pt on WO_{3-x} for utilization of Pt in the hydrogen evolution reaction, Angew. Chem. Int. Ed. 58 (2019) 16038–16042.

[9] X. Sui, L. Zhang, J. Li, K. Doyle-Davis, R. Li, Z. Wang, X. Sun, Advanced support materials and interactions for atomically dispersed noble-metal catalysts: from support effects to design strategies, Adv. Energy Mater. 12 (2022) 2102556.

[10] Z. Li, R. Wu, L. Zhao, P.B. Li, X.X. Wei, J.J. Wang, J.S. Chen, T.R. Zhang, Metal-support interactions in designing noble metal-based catalysts for electrochemical CO₂ reduction: recent advances and future perspectives, Nano Res. 14 (2021) 3795–3809.

[11] B.J. Hsieh, M.C. Tsai, C.J. Pan, W.N. Su, J. Rick, J.F. Lee, Y.W. Yang, B.J. Hwang, Platinum loaded on dual-doped TiO₂ as an active and durable oxygen reduction reaction catalyst, NPG Asia Mater. 9 (2017), e403.

[12] C. Jackson, G.T. Smith, D.W. Inwood, A.S. Leach, P.S. Whalley, M. Callisti, T. Polcar, A.E. Russell, P. Levecque, D. Kramer, Electronic metal-support interaction enhanced oxygen reduction activity and stability of boron carbide supported platinum, Nat. Commun. 8 (2017) 15802.

[13] Y. Shi, Z.R. Ma, Y.Y. Xiao, Y.C. Yin, W.M. Huang, Z.C. Huang, Y.Z. Zheng, F.Y. Mu, R. Huang, G.Y. Shi, Y.Y. Sun, X.H. Xia, W. Chen, Electronic metal-support interaction modulates single-atom platinum catalysis for hydrogen evolution reaction, Nat. Commun. 12 (2021) 3021.

[14] X. Xie, Y. Xue, L. Li, S. Chen, Y. Nie, W. Ding, Z. Wei, Surface Al leached Ti₃AlC₂ as a substitute for carbon for use as a catalyst support in a harsh corrosive electrochemical system, Nanoscale 6 (2014) 11035–11040.

[15] J. Yang, W.H. Li, S. Tan, K. Xu, Y. Wang, D. Wang, Y. Li, The electronic metal-support interaction directing the design of single atomic site catalysts: achieving high efficiency towards hydrogen evolution, Angew. Chem. Int. Ed. 60 (2021) 19085–19091.

[16] S.J. Tauster, S.C. Fung, R.L. Garten, Strong metal-support interactions. Group 8 noble metals supported on TiO₂, J. Am. Chem. Soc. 100 (1978) 170–175.

[17] Q. Cheng, Y. Liu, S. Lyu, Y. Tian, Q. Ma, X. Li, Manipulating metal-support interactions of metal catalysts for Fischer-Tropsch synthesis, Chin. J. Chem. Eng. 35 (2021) 220–230.

[18] J. Liu, L. Wang, F. Okejiri, J. Luo, J. Zhao, P. Zhang, M. Liu, S. Yang, Z. Zhang, W. Song, W. Zhu, J. Liu, Z. Zhao, G. Feng, C. Xu, S. Dai, Deep understanding of strong metal interface confinement: a journey of Pd/FeOx catalysts, ACS Catal. 10 (2020) 8950–8959.

[19] S. Li, Y. Xu, Y.F. Chen, W. Li, L. Lin, M. Li, Y. Deng, X. Wang, B. Ge, C. Yang, S. Yao, J. Xie, Y. Li, X. Liu, D. Ma, Tuning the selectivity of catalytic carbon dioxide hydrogenation over iridium/cerium oxide catalysts with a strong metal-support interaction, Angew. Chem. Int. Ed. 56 (2017) 10761–10765.

[20] Y. Zhang, W. Yan, H. Qi, X. Su, Y. Su, X. Liu, L. Li, X. Yang, Y. Huang, T. Zhang, Strong metal-support interaction of Ru on TiO₂ derived from the Co-reduction mechanism of RuxTi₁₋xO₂ interphase, ACS Catal. 12 (2022) 1697–1705.

[21] M.G. Willinger, W. Zhang, O. Bondarchuk, S. Shaikhutdinov, H.J. Freund, R. Schlogl, A case of strong metal-support interactions: combining advanced microscopy and model systems to elucidate the atomic structure of interfaces, Angew. Chem. Int. Ed. 53 (2014) 5998–6001.

[22] A. Beck, X. Huang, L. Artiglia, M. Zabilskiy, X. Wang, P. Rzepka, D. Palagin, M. G. Willinger, J.A. van Bokhoven, The dynamics of overlayer formation on catalyst nanoparticles and strong metal-support interaction, Nat. Commun. 11 (2020) 3220.

[23] F. Polo-Garzon, T.F. Blum, Z. Bao, K. Wang, V. Fung, Z. Huang, E.E. Bickel, D. Jiang, M. Chi, Z. Wu, In situ strong metal-support interaction (SMSI) affects catalytic alcohol conversion, ACS Catal. 11 (2021) 1938–1945.

[24] M. Luo, S. Guo, Strain-controlled electrocatalysis on multimetallic nanomaterials, Nat. Rev. Mater. 2 (2017) 17059.

[25] X.X. Wang, J. Sokolowski, H. Liu, G. Wu, Pt alloy oxygen-reduction electrocatalysts: synthesis, structure, and property, Chin. J. Catal. 41 (2020) 739–755.

[26] T.W. van Deelen, C. Hernández Mejía, K.P. de Jong, Control of metal-support interactions in heterogeneous catalysts to enhance activity and selectivity, Nat. Catal. 2 (2019) 955–970.

[27] S. Zhang, P.N. Plessow, J.J. Willis, S. Dai, M. Xu, G.W. Graham, M. Cargnello, F. Abild-Pedersen, X. Pan, Dynamical observation and detailed description of catalysts under strong metal-support interaction, Nano Lett. 16 (2016) 4528–4534.

[28] L. Wang, L. Wang, X. Meng, F.S. Xiao, New strategies for the preparation of sinter-resistant metal-nanoparticle-based catalysts, Adv. Mater. 31 (2019) 1901905.

[29] J. Zhang, H. Wang, L. Wang, S. Ali, C. Wang, L. Wang, X. Meng, B. Li, D.S. Su, F.-S. Xiao, Wet-chemistry strong metal–support interactions in Titania-supported Au catalysts, J. Am. Chem. Soc. 141 (2019) 2975–2983.

[30] J. Zhang, D. Zhu, J. Yan, C.-A. Wang, Strong metal-support interactions induced by an ultrafast laser, Nat. Commun. 12 (2021) 6665.

[31] J. Zhang, J. Ma, T.S. Choksi, D. Zhou, S. Han, Y.-F. Liao, H.B. Yang, D. Liu, Z. Zeng, W. Liu, X. Sun, T. Zhang, B. Liu, Strong metal–support interaction boosts activity, selectivity, and stability in electrosynthesis of H₂O₂, J. Am. Chem. Soc. 144 (2022) 2255–2263.

[32] F. Yang, H. Zhao, W. Wang, L. Wang, L. Zhang, T. Liu, J. Sheng, S. Zhu, D. He, L. Lin, J. He, R. Wang, Y. Li, Atomic origins of the strong metal-support interaction in silica supported catalysts, Chem. Sci. 12 (2021) 12651–12660.

[33] S. Wang, K. Feng, D. Zhang, D. Yang, M. Xiao, C. Zhang, L. He, B. Yan, G.A. Ozin, W. Sun, Stable Cu catalysts supported by two-dimensional SiO₂ with strong metal-support interaction, Adv. Sci. 9 (2022) 2104972.

[34] C. Yang, Y. Lu, L. Zhang, Z. Kong, T. Yang, L. Tao, Y. Zou, S. Wang, Defect engineering on CeO₂-based catalysts for heterogeneous catalytic applications, Small Struct. 2 (2021) 2100058.

[35] Y. Wang, Z. Chen, P. Han, Y. Du, Z. Gu, X. Xu, G. Zheng, Single-atomic Cu with multiple oxygen vacancies on Ceria for electrocatalytic CO₂ reduction to CH₄, ACS Catal. 8 (2018) 7113–7119.

[36] M.K. Carpenter, T.E. Moylan, R.S. Kukreja, M.H. Atwan, M.M. Tessema, Solvothermal synthesis of platinum alloy nanoparticles for oxygen reduction electrocatalysis, J. Am. Chem. Soc. 134 (2012) 8535–8542.

[37] R. Chattot, O. Le Bacq, V. Beermann, S. Kuhl, J. Herranz, S. Henning, L. Kuhn, T. Asset, L. Guetaz, G. Renou, J. Drnec, P. Bordet, A. Pasturel, A. Eychmuller, T. J. Schmidt, P. Strasser, L. Dubau, F. Maillard, Surface distortion as a unifying concept and descriptor in oxygen reduction reaction electrocatalysis, Nat. Mater. 17 (2018) 827–833.

[38] Q. Chang, Y. Hong, H.J. Lee, J.H. Lee, D. Ologunagba, Z. Liang, J. Kim, M.J. Kim, J. W. Hong, L. Song, S. Kattel, Z. Chen, J.G. Chen, S.-I. Choi, Achieving complete electrooxidation of ethanol by single atomic Rh decoration of Pt nanocubes, Proc. Natl. Acad. Sci. USA 119 (2022), e2112109119.

[39] L. Zhao, R. Wu, J. Wang, Z. Li, X. Wei, J.S. Chen, Y. Chen, Synthesis of noble metal-based intermetallic electrocatalysts by space-confined pyrolysis: recent progress and future perspective, J. Energy Chem. 60 (2021) 61–74.

[40] X. Liu, S. Jia, M. Yang, Y. Tang, Y. Wen, S. Chu, J. Wang, B. Shan, R. Chen, Activation of subnanometric Pt on Cu-modified CeO₂ via redox-coupled atomic layer deposition for CO oxidation, Nat. Commun. 11 (2020) 4240.

[41] Q. Wang, S. Chen, P. Li, S. Ibraheem, J. Li, J. Deng, Z. Wei, Surface Ru enriched structurally ordered intermetallic PtFe@PtRuFe core-shell nanostructure boosts methanol oxidation reaction catalysis, Appl. Catal. B Environ. 252 (2019) 120–127.

[42] X. Zou, S. Chen, Q. Wang, X. Gao, J. Li, J. Li, L. Li, W. Ding, Z. Wei, Leaching- and sintering-resistant hollow or structurally ordered intermetallic PtFe alloy catalysts for oxygen reduction reactions, Nanoscale 11 (2019) 20115–20122.

[43] T. He, W. Wang, F. Shi, X. Yang, X. Li, J. Wu, Y. Yin, M. Jin, Mastering the surface strain of platinum catalysts for efficient electrocatalysis, Nature 598 (2021) 76–81.

[44] A. Nilsson, L.G.M. Pettersson, B. Hammer, T. Bligaard, C.H. Christensen, J. K. Nørskov, The electronic structure effect in heterogeneous catalysis, Catal. Lett. 100 (2005) 111–114.

[45] M. Asano, R. Kawamura, R. Sasakawa, N. Todoroki, T. Wadayama, Oxygen reduction reaction activity for strain-controlled Pt-based model alloy catalysts: surface strains and direct electronic effects induced by alloying elements, ACS Catal. 6 (2016) 5285–5289.

[46] Y. Zhou, D. Liu, Z. Liu, L. Feng, J. Yang, Interfacial Pd-O-Ce linkage enhancement boosting formic acid electrooxidation, ACS Appl. Mater. Interfaces 12 (2020) 47065–47075.

[47] Y. Nie, Y. Wang, X. Zheng, T. Yang, Q. Wen, Y. Fang, X. Cheng, R. Li, L. Li, Minutely surficial functionalization of Ce-O-Pt linkages on Pt/C for enhanced electrocatalytic methanol oxidation, Appl. Surf. Sci. 602 (2022), 154194.

[48] X. Du, Y. Huang, X. Pan, B. Han, Y. Su, Q. Jiang, M. Li, H. Tang, G. Li, B. Qiao, Size-dependent strong metal-support interaction in TiO₂ supported Au nanocatalysts, Nat. Commun. 11 (2020) 5811.

[49] J. Liu, L. Wang, F. Okejiri, J. Luo, J. Zhao, P. Zhang, M. Liu, S. Yang, Z. Zhang, W. Song, W. Zhu, J. Liu, Z. Zhao, G. Feng, C. Xu, S. Dai, Deep understanding of strong metal interface confinement: a journey of Pd/FeOx catalysts, ACS Catal. 10 (2020) 8950–8959.

[50] S. Zhang, Z. Zeng, Q. Li, B. Huang, X. Zhang, Y. Du, C.-H. Yan, Lanthanide electronic perturbation in Pt–Ln (La, Ce, Pr and Nd) alloys for enhanced methanol oxidation reaction activity, Energy Environ. Sci. 14 (2021) 5911–5918.

[51] L. Peng, X. Zheng, L. Li, L. Zhang, N. Yang, K. Xiong, H. Chen, J. Li, Z. Wei, Chimney effect of the interface in metal oxide/metal composite catalysts on the hydrogen evolution reaction, Appl. Catal. B Environ. 245 (2019) 122–129.

[52] Z. Zhang, J. Li, S. Liu, X. Zhou, L. Xu, X. Tian, J. Yang, Y. Tang, Self-templating-oriented manipulation of ultrafine Pt₃Cu alloyed nanoparticles into asymmetric porous bowl-shaped configuration for high-efficiency methanol electrooxidation, Small 18 (2022) 2202782.

[53] L. Hui, Y. Xue, C. Xing, Y. Liu, Y. Du, Y. Fang, H. Yu, C. Zhang, F. He, Y. Li, Atomic alloys of nickel-platinum on carbon network for methanol oxidation, Nano Energy 95 (2022), 106984.

[54] F. Wu, K. Eid, A.M. Abdullah, W. Niu, C. Wang, Y. Lan, A.A. Elzatahry, G. Xu, Unveiling one-pot template-free fabrication of exquisite multidimensional PtNi multicube nanoarchitectonics for the efficient electrochemical oxidation of ethanol and methanol with a great tolerance for CO, ACS Appl. Mater. Interfaces 12 (2020) 31309–31318.

[55] N. Markovic, H. Gasteiger, P.N. Ross, Kinetics of oxygen reduction on Pt(hkl) electrodes: implications for the crystallite size effect with supported Pt electrocatalysts, J. Electrochem. Soc. 144 (1997) 1591.

[56] G. Fu, X. Yan, Z. Cui, D. Sun, L. Xu, Y. Tang, J.B. Goodenough, J.M. Lee, Catalytic activities for methanol oxidation on ultrathin CuPt₃ wavy nanowires with/without smart polymer, Chem. Sci. 7 (2016) 5414–5420.

[57] C. Li, T. Liu, T. He, B. Ni, Q. Yuan, X. Wang, Composition-driven shape evolution to Cu-rich PtCu octahedral alloy nanocrystals as superior bifunctional catalysts for methanol oxidation and oxygen reduction reaction, Nanoscale 10 (2018) 4670–4674.

[58] F. Lin, Y. Sun, J. Lai, K. Wang, Y. Tang, Y. Chao, Y. Yang, J. Feng, F. Lv, P. Zhou, M. Huang, S. Guo, 3D PtFe clusters with cube-in-cube structure enhance oxygen reduction catalysis and electrochemical sensing, Small Methods 2 (2018) 1800073.

[59] M. Xu, S. Yao, D. Rao, Y. Niu, N. Liu, M. Peng, P. Zhai, Y. Man, L. Zheng, B. Wang, B. Zhang, D. Ma, M. Wei, Insights into interfacial synergistic catalysis over Ni@ TiO₂₋x catalyst toward water–gas shift reaction, J. Am. Chem. Soc. 140 (2018) 11241–11251.

[60] J. Greeley, M. Mavrikakis, Alloy catalysts designed from first principles, Nat. Mater. 3 (2004) 810–815.

[61] X. Zheng, L. Li, M. Deng, J. Li, W. Ding, Y. Nie, Z. Wei, Understanding the effect of interfacial interaction on metal/metal oxide electrocatalysts for hydrogen evolution and hydrogen oxidation reactions on the basis of first-principles calculations, Catal. Sci. Technol. 10 (2020) 4743–4751.

[62] Y. Qin, W. Zhang, K. Guo, X. Liu, J. Liu, X. Liang, X. Wang, D. Gao, L. Gan, Y. Zhu, Z. Zhang, W. Hu, Fine-tuning intrinsic strain in Penta-twinned Pt–Cu–Mn nanoframes boosts oxygen reduction catalysis, Adv. Funct. Mater. 30 (2020) 1910107.

[63] W. Li, D. Wang, T. Liu, L. Tao, Y. Zhang, Y.C. Huang, S. Du, C.L. Dong, Z. Kong, Yf Li, S. Lu, S. Wang, Doping-modulated strain enhancing the phosphate tolerance on PtFe alloys for high-temperature proton exchange membrane fuel cells, Adv. Funct. Mater. 32 (2021) 2109244.

[64] C. Liu, L. Zhang, L. Sun, W. Wang, Z. Chen, Enhanced electrocatalytic activity of PtCu bimetallic nanoparticles on CeO_2/carbon nanotubes for methanol electro-oxidation, Int. J. Hydrog. Energy 45 (2020) 8558–8567.

[65] L. Chen, X. Liang, X. Li, J. Pei, H. Lin, D. Jia, W. Chen, D. Wang, Y. Li, Promoting electrocatalytic methanol oxidation of platinum nanoparticles by cerium modification, Nano Energy 73 (2020), 104784.